Modelling of SOEC-FT reactor: pressure effects on methanation process

Bin Chen, Haoran Xu, Meng Ni[*]

Building Energy Research Group, Department of Building and Real Estate, The Hong Kong Polytechnic University, Hung Hom, Kowloon, Hong Kong

Abstract

In this paper a numerical model is developed for a novel reactor combining a Solid Oxide Electrolyzer Cell (SOEC) section with a Fischer Tropsch like section for methane production under pressurized & temperature-gradient condition. Governing equations for mass, momentum, charge transport are solved with Finite Element Method. The chemical reaction kinetics of reversible water gas shift reaction and reversible methanation reaction in Ni/YSZ cathode are fully considered. The model is validated by comparing simulation results with experimental data. Parametric simulations are conducted to understand the physical-chemical processes in the reactor with a focus on the pressure effect. It is predicted that the optimal operating pressure is around 3 bar, beyond which the CH_4 conversion ratio (2.5 times enhanced than 1 bar operating) cannot be further increased. It is also found that it is feasible to operate the pressurized SOEC at a lower temperature for CH_4 production with improved catalyst activity.

---

[*] Corresponding author:
Email: meng.ni@polyu.edu.hk
Tel: 852-27664152; Fax: 852-27645131

## 1. Introduction

The Solid Oxide Electrolysis Cell (SOEC) is a high temperature electrochemical device that can efficiently convert H_2O/CO_2 to syngas using excess renewable power. The advantages of SOEC include high efficiency, applicability to distributed systems and inlet gas flexibility [1]. Co-electrolysis of H_2O/CO_2 by SOEC technology is becoming an attractive option for fuel production, CO_2 utilization and renewable electricity storage in recent years [2-6]. Methane production using SOEC is an interesting research area for useful fuel production from steam and captured carbon dioxide. Some preliminary experimental and theoretical analysis have been conducted on SOEC for methane generation. Li et al. [7] experimentally discussed the methane production mechanism in SOEC from 550°C to 750°C at 1 bar. Very low methane production rate was achieved at a high operating voltage (2 V). Hansen et al. [8] developed several processes for converting biogas to CH_4 rich gas using SOEC after mixing H_2O and CO_2, followed by methanation process. JP. Stempien, et al. [9] thermodynamically assessed the methane production by SOEC considering Sabatier reaction and methane steam reforming reaction. C. Schlitzberger et al. [10] proposed a novel two tank chemical storage system combining SOFC and SOEC for the CO_2 capture and methane production. T. Kato et al. [11] compared the methanation performance of SOEC and traditional water electrolyser + methanator system. It is found that the SOEC methanation system shows higher conversion rate and higher energy efficiency. C. Wendel et al. [12] proposed a SOEC+SOFC battery system, holding the view that methanation in SOEC is preferable due to the increased energy storage capacity, better thermal management (lower thermoneutral voltage), and the mitigated carbon deposition. G. Botta et, al. [13] analysed the methane content in a dimethyl ether synthesis process using syngas produced from SOEC by H_2O and CO_2 co-electrolysis.

The working principle of co-electrolysis process in SOEC cathode can be written as two electrochemical reactions:

2

$$H_2O + 2e^- \rightarrow H_2 + O^{2-} \tag{1}$$

$$CO_2 + 2e^- \rightarrow CO + O^{2-} \tag{2}$$
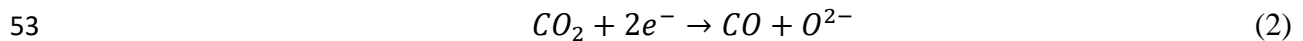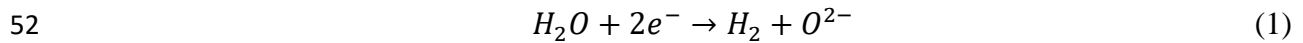
54 The oxygen ions come from the anode side by oxygen electrochemical reduction:

$$\frac{1}{2}O_2 \rightarrow 2e^- + O^{2-} \tag{3}$$
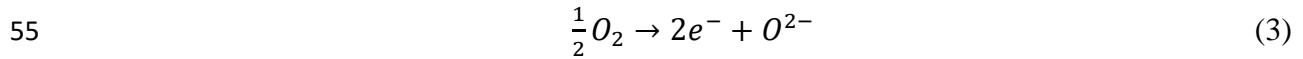
56 Furthermore, two main chemical reactions (methane steam reforming and waster gas shift

57 reaction) can also take place inside the SOEC cathode, as the usually used Nickel catalyst in

58 the cathode shows good catalytic activity towards these two chemical reactions.

59 Products (the exit gas mixed) of SOEC usually contain H_2/CO rich mixture (syngas) with un-

60 reacted H_2O and CO_2. The syngas can be used for power generation by conventional thermal

61 power plants via combustion or by Solid Oxide Fuel Cells (SOFCs, reversed operation of

62 SOEC) via electrochemical reactions. The reversibility of the solid oxide cell (SOEC mode or

63 SOFC mode) enables conversion between electricity and fuels. Thus SOFC/SOEC system can

64 be used for energy storage [14, 15]. In addition, the syngas produced from SOEC co-

65 electrolysis can be further processed by Fischer-Tropsch (FT) reactors for production of liquid

66 fuels or chemicals, which are easy to transport and store and thus more suitable for distributed

67 systems [16-18].

68 The FT process is well-established in the industry for fuel production in the temperature range

69 of 150-350 ºC and pressure up to several tens of bar [19]. The products of traditional FT

70 process is a variety of hydrocarbons in the form of C_nH_{2n+2}, where n is in the range of $1 < n < 30$.

71 Since SOEC and FT reactors are operated at very different temperatures and pressures, the

72 SOEC + FT systems are usually designed as 2 separate reactors: (1) SOEC at high temperature

73 and ambient pressure and (2) FT reactor at lower temperature but high pressure [9, 20].

74   Recently, a novel design combining SOEC (800 ℃) and methanation reactor (FT-like) at low

75   temperature (250 ℃) in one tubular reactor to produce hydrocarbon (mainly CH_4) has been

76   proposed and demonstrated to be feasible by Chen Long et al [21]. The newly developed one-

77   step SOEC-FT system is compact and relatively easy to fabricate.

78   The FT-like reactor at downstream adopts Nickel as the catalyst to converse the CO/H_2 rich

79   gas from the SOEC section to CH_4 in a region cooling from 800℃ to 250℃. To the best

80   knowledge of the authors, there is very limited research works on this one-step SOEC-FT

81   reactor operated under ambient pressure [21, 22]. And there is still no report about the

82   pressurized SOEC-FT reactor.

83   Considering that increasing the operating pressure is not only helpful for the methane

84   production in SOECs (see refs. [23] and [24]), but also benefiting the FT-like process, it is

85   necessary to study the pressurized SOEC-FT design (see Fig. 1). Therefore, in this paper, the

86   previously developed model is further extended to study the pressure effects on the SOEC-FT

87   reactor performance which is the new contribution of this paper.

88

89   **2. Model development**

90   This multi-physics model developed in this paper is extended from our previous model for

91   ambient SOEC-FT reactor and already well validated with experimental data [21] and reported

92   in previous work [22]. To be concise, the model is only briefly introduced in this section.

93   Figure 1 shows the schematics of the SOEC-FT reactor with 2 sections. Reactor's geometrical

94   parameters can be found in Table 1. The whole reactor is a typical tubular SOEC section (on

95   the left) connected with an FT-like section (placed in a cooling temperature zone on the right

96   side). In the base case operation, the SOEC section works at 800 ℃ while the FT-like section

97   cools down from 800 ℃ to 250 ℃ (temperature at the outlet). The SOEC consists of 3 layers:

98   a supporting cathode layer (Ni/YSZ), a dense YSZ electrolyte layer in between and an anode

99   layer (LSM/YSZ), which is printed on the outer surface of the SOEC section. A voltage of

100   1.3V is applied to the SOEC section for H_2O/CO_2 co-electrolysis. For the FT part, as no anode

101   layer is deposited on YSZ, the co-electrolysis process is negligible in this section. Therefore,

102   only the reversible methane steam reforming (MSR) reaction (reversed methanation) as Eq. 4

103   and reversible water gas shift reaction (WGSR) as Eq. 5 are considered in the FT section:

$$CH_4 + H_2O \leftrightarrow CO + 3H_2 \tag{4}$$
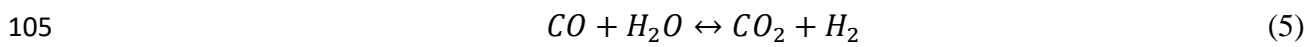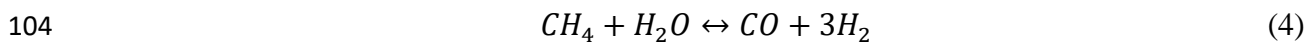
$$CO + H_2O \leftrightarrow CO_2 + H_2 \tag{5}$$

106   In the operation, the inlet gas composition is fixed at $H_2O/CO_2/H_2$ = 0.2/0.175/0.625, which is

107   an optimal value for SOEC-FT reactor operating at ambient pressure, based on our previous

108   modelling work [22]. The H_2O and CO_2 are co-electrolysed in the SOEC section to increase

109   the content of H_2 and CO. Then the gas mixture subsequently enters the FT-like section, where

110   methanation reaction (reversed MSR) is activated to produce CH_4. Finally, the outlet gas

111   composition will be analysed to evaluate the reactor's methanation process. Outside of the tube,

112   compressed air is swept to carry away the oxygen generated in the SOEC section. The overall

113   reactor is operated under 1 bar to 5 bar so that the pressure effect can be parametrically studied.

114   The reactor involves highly coupled multi-physical processes. Finite element method is

115   employed to discretize the governing equations for the charge transport, momentum transport

116   and mass transport, then solved by iterative MUMPS method [25]. The formulations of the

117   three coupled physical fields are summarized below.

118   **2.1 Charge transport model**

119   Definition and values for variables used in equations (6)-(31) can be found in the Nomenclature.

120   The charge transport is governed by the Ohm's law, from which two electrical potentials and

121   local current density can be calculated:

122 $\quad i_l = -\sigma_l{}^{eff}\nabla(\emptyset_l)$ (6)

123 $\quad i_s = -\sigma_{s.eff}\nabla(\emptyset_s)$ (7)

124   where $\emptyset_l$ and $\emptyset_s$ are ionic phase potential and electronic phase potential respectively for the

125   two charge conducting phases used in the SOEC. As the electron conduction in the YSZ

126   electrolyte is negligible, the electrolyte is assumed to be purely ion-conducting media, thus

127   only $\emptyset_l$ distribution in the electrolyte is considered. Due to the dual conducting character of

128   the composite electrodes, both $\emptyset_l$ and $\emptyset_s$ are applied to the electrode layer. The effective

129   conductivity of each phase noted as $\sigma_{s(l)}{}^{eff}$, is calculated in consideration of intrinsic material

130   and microstructure characters by the following correction equations:

131 $\quad \sigma_l{}^{eff} = \sigma_l \cdot \dfrac{V_{YSZ}}{\tau_{YSZ}}$ (8)

132 $\quad \sigma_{s,a}{}^{eff} = \sigma_{s.LSM} \cdot \dfrac{V_{LSM}}{\tau_{LSM}}$ (9)

133 $\quad \sigma_{s,c}{}^{eff} = \sigma_{s.Ni} \cdot \dfrac{V_{Ni}}{\tau_{Ni}}$ (10)

134   It should be mentioned that more comprehensive expressions for the effective conductivity can

135   be derived from more fundamental methods such as Percolation theory, random packing model,

136   etc. The effective conductivity may also differ for the electrodes with different particles sizes,

137   due to different fabrication techniques (e.g. Infiltration/mechanical mixing). The employed

138   simplification expressions are considered reasonably accurate. Detailed expressions for the

139   intrinsic conductivities ($\sigma_l, \sigma_{s.Ni}$ and $\sigma_{s.LSM}$) are shown below [22]:

140 $\quad \sigma_l = 33.4E3 \cdot exp(-10300 \cdot T^{-1})$ (11)

141 $\quad \sigma_{s.LSM} = 4.2E7 \cdot T^{-1} \cdot exp(-1200 \cdot T^{-1})$ (12)

142 $\quad \sigma_{s.Ni} = 9.5E7 \cdot T^{-1} \cdot exp(-1150 \cdot T^{-1})$ (13)

143   The potential difference between the two phases can be calculated from the applied local Nernst

144   equilibrium potential and local overpotentials:

145    $\emptyset_l - \emptyset_s = E - \eta_{act}$ (14)

146   Since there are two electrochemical reaction paths in the co-electrolysis processes, two

147   equilibrium Nernst potentials for the H$_2$O reduction (E_{H_2O}) and CO$_2$ reduction (E_{CO_2}) are used

148   in the electrochemical model in a parallel manner [26]:

149    $E_{H_2O} = 1.253 - 0.00024516T + \dfrac{RT}{2F} \ln\left[\dfrac{P_{H_2}(P_{O_2})^{0.5}}{P_{H_2O}^I}\right]$ (15)

150    $E_{CO_2} = 1.46713 - 0.0004527T + \dfrac{RT}{2F} \ln\left[\dfrac{P_{CO}(P_{O_2})^{0.5}}{P_{CO_2}}\right]$ (16)

151   The Ohmic overpotential is explicitly included in the Ohm's law (Eq. 6~7), and the

152   concentration overpotential is implicitly included in the local equilibrium potentials as the

153   mixture constituents partial pressures at the electrode-electrolyte interface are used (Eq.

154   15&16). Besides, the activation polarization ($\eta_{act.a(c)}$) in the anode and cathode can be

155   obtained from widely used Butler–Volmer equations [27]:

156    $i_a = AV_a \cdot i_{o,a}\left(exp\left(\dfrac{0.5F\cdot\eta_{act.a}}{RT}\right) - exp\left(\dfrac{-0.5F\cdot\eta_{act.a}}{RT}\right)\right)$ (17)

157    $i_{c,H_2O} = AV_c \cdot i_{o,H_2O}\left(\dfrac{p_{H_2}}{p_{H_2,ref}}exp\left(\dfrac{0.5F\cdot\eta_{act.a}}{RT}\right) - \dfrac{p_{H_2O}}{p_{H_2O_{.ref}}}exp\left(\dfrac{-0.5F\cdot\eta_{act.a}}{RT}\right)\right)$ (18)

158    $i_{c,CO_2} = AV_c \cdot i_{o,CO_2}\left(\dfrac{p_{CO}}{p_{CO_{ref}}}exp\left(\dfrac{0.5F\cdot\eta_{act.a}}{RT}\right) - \dfrac{p_{CO_2}}{p_{CO_{2.ref}}}exp\left(\dfrac{-0.5F\cdot\eta_{act.a}}{RT}\right)\right)$ (19)

159   **2.2 Chemical model formulation**

160   It is noted that the kinetics of chemical reactions vary greatly with operating conditions.

161   Therefore, for a real FT-like reactor, the kinetic modelling for the hydrocarbonisation reactions

162   is quite challenging since the processes highly depend on the type of catalyst, structure,

163   temperature and pressure [28]. However, the catalyst used in the FT-like section in the present

164   study is Nickel and YSZ composite which is well studied and demonstrated to be reliable by

165   Haberman and Young [29]. Both reversible WGSR and reversible MSR reactions are assumed

166   to take place in the cathode porous layer. This assumption has been validated in the previous

167   works [22, 30] for solid oxide cell applications with $H_2/CO/H_2O/CO_2$ gas system as feeding

168   gas. The following are the rate expressions employed for these two reactions [29]:

169     $R_{WGSR} = K_{sf} \left(p_{H_2O} p_{CO} - \frac{p_{H_2} p_{CO_2}}{K_{ps}} \right) (mol\ m^{-3} s^{-1})$ (20)

170     $K_{sf} = 0.0171\ exp \left(\frac{-103191}{RT} \right) (mol\ m^{-3} Pa^{-2} s^{-1})$ (21)

171     $K_{ps} = \exp(-0.2935Z^3 + 0.6351Z^2 + 4.1788Z + 0.3169)$ (22)

172     $R_{MSR} = K_{rf} \left(p_{CH_4} p_{H_2O} - \frac{p_{CO}(p_{H_2})^3}{K_{pr}} \right) (mol\ m^{-3} s^{-1})$ (23)

173     $K_{rf} = 2395\ exp \left(\frac{-231266}{RT} \right) (mol\ m^{-3} Pa^{-2} s^{-1})$ (24)

174     $K_{pr} = 1.027E10 \times \exp(-0.2513Z^4 + 0.36651Z^3 + 0.5810Z^2 - 27.134Z + 3.277)$ (25)

175     $Z = \frac{1000}{T(K)} - 1$ (26)

176   **2.3 CFD model formulation**

177   To simulate the multi-species gas transport in the flow channels and porous layers, the

178   conservation laws for mass, momentum, and species are coupled and solved simultaneously.

179   Mass conservation:

180     $\nabla(\rho U) = S_m$ (0 for gas channel)   (27)

181   Momentum conservation for gas channel:

182 $$\rho\big((U \cdot \nabla)U\big) = \nabla \cdot \left[-p + \mu(\nabla U + (\nabla U)^T) - \frac{2}{3}\mu(\nabla \cdot U)\right] + F_{vol} \tag{28}$$

183 Momentum conservation for porous flow:

184 $$\frac{\rho}{\epsilon}\left((U \cdot \nabla)\frac{U}{\epsilon}\right) = \nabla \cdot \left[-p + \frac{\mu(\nabla U + (\nabla U)^T)}{\epsilon} - \frac{2}{3}\frac{\mu}{\epsilon}(\nabla \cdot U)\right] - \big(\mu\kappa^{-1} + \nabla(\rho U)\big)U + F_{vol} \tag{29}$$

185 Species conservation for gas channel:

186 $$\nabla\left(-\rho \cdot w_i \sum_{j \neq i}^{n} D_{ij} \nabla x_j + \big(x_j - w_j\big) \cdot \nabla p \cdot p^{-1} \cdot U\right) + \rho \cdot U \cdot \nabla w_j = 0 \tag{30}$$

187 Species conservation for porous flow:

188 $$\nabla\left(-\rho \cdot w_i \sum_{j \neq i}^{n} D_{eff,ij} \nabla x_j + \big(x_j - w_j\big) \cdot \nabla p \cdot p^{-1} \cdot U\right) + \rho \cdot U \cdot \nabla w_j = S_i + R_i \tag{31}$$

189 where the interpretation of all the variables and constants above can be found in Nomenclature.

190 To reflect the reactions' effects on the fluid flow, species' generation rate or consumption rate

191 by chemical or electrochemical reactions are included as source terms on the right side of the

192 conservation equations (Eq. 27 & 31). Assumptions for the CFD model are summarized and

193 listed below:

194   (1) Gas flows are all incompressible laminar flow

195   (2) All gases behave as ideal gas

196   (3) Darcy-Brinkman correction is used to formulate the flow in the porous layer on the

197   momentum transport [31]

198   (4) Dusty gas model is used for the effective diffusion coefficients [32]

199 **2.4 Temperature settings**

200 The temperature condition of this combined SOEC-FT system is set manually by the furnace

201 to achieve the desired temperature distribution in experiments. For instance, Case IV of L.

202 Chen's work [21]: the temperature is assumed to be uniform at 800 ℃ in the whole SOEC

203   section and then gradually cools down in the FT-like section to 250 ℃ at the outlet. Similarly

204   in this study, the temperature of FT-like section is assumed to be linearly distributed. In real

205   applications, the thermoneutral design is preferred as extra heat supplier or cooler could be

206   removed from the reactor hotbox. In the case of SOEC-FT reactor, the exothermic methanation

207   process is more dominating so that the electrolysis voltage should be slightly lower than the

208   typical thermoneutral voltage (between 1.29 V and 1.46V [33]) to balance the heat flux. The

209   authors regret to point that the analysis of heat management by integrating the heat transfer

210   sub-model is to be investigated in the future works.

211   **2.5 Boundary conditions**

212   For the transport of ions and electrons, the potential of electron phase at the upper-surface of

213   the anode is assumed to be uniform and equal to the operating voltage ($Vcell$). On the other

214   side, the inner-surface of the cathode layer is accordingly grounded. For the mass and

215   momentum transport, the volumetric flow rate at the inlet is 18.9 ml/min, and outlet pressure

216   is set as the operating pressure. The inlet gas composition is shown in Table 1. It should be

217   noted that the high inlet H_2 mole fraction is employed to sustain the reducing environment at

218   the cathode side to avoid the oxidation of Nickel particles. The H_2 in the outlet gas after CH_4

219   removal (63.3% mole fraction at 1 bar of Fig. 4) should be recirculated to the inlet so that the

220   targeted H_2 mole fraction (i.e. 62.47%) can be maintained at the inlet. For high pressure

221   operating cases (P_{op} >1 bar), the H_2 consumption is large that the H_2 mole fraction cannot be

222   compensated only by recirculating. Increasing the operating voltage and decreasing the

223   prescribed inlet H_2 mole fraction could be considerable in real applications.

224   **3.   Results and discussion**

225   The model is capable of simulating the reactor under conditions defined by various

226   combinations of the operating variables, including pressure, temperature, voltage, and different

227   electrode activity. The sensitivity studies of those parameters will be conducted according to

228　the settings in Table 2. The operating parameters for the basic case is referred from the testing

229　parameters of the reactor prototype with the optimized inlet gas composition optimization [21,

230　22].

231　Case 1 investigate the pressure effects on the reactor, with P_{op} ranging from 1 bar to 5 bar and

232　other parameters fixed as same as the basic case. For the temperature sensitivity (Case 2), one

233　of the SOEC section temperature (T_{SOFC}) and FT-like section outlet temperature (T_{FT}) are

234　changed with the other fixed, to reduce the computational workload. The range of T_{SOFC} is set

235　as 600 ℃ to 1000 ℃, which covers the typical SOEC working temperature. The range of T_{FT}

236　is set below the T_{SOFC} and above 200 ℃ to see the reactor methanation performance in the wide

237　range. Too low T_{FT} is not preferred since the methane production is not expected to increase

238　due to the low rate of reversed MSR reaction.

239　Case 3 focuses on the operating voltage, which ranges from 1.2 V to 2.0 V. Since the increase

240　of voltage will preferably improve the fraction of H_2/CO by co-electrolysis at the cost of

241　increased electricity input, the upper limit of the simulation range (2.0 V) is high enough to

242　help investigate the reactor's response to the different amount of renewable energy input.

243　Case 4 is to help assess the feasibility of this reactor in the light of material development when

244　electrode materials are expected to show higher exchange current density than typical values.

245　The original i_{o,H_2O}(5300 Am^{-2}, 800 ℃), i_{o,CO_2}(1590 Am^{-2}, 800 ℃) and $i_{o,a}$(2000Am^{-2}, 800 ℃)

246　[30] are the exchange current densities for co-electrolysis reactions and oxygen reduction

247　reaction. These three parameters will be increased at the same enlargement ratio, up to 3 times,

248　so as to show the effects of high performance electrode on the reactor."

3.1. Pressure effects on conversion ratio of CH_4

250　The main results of the Case 1 include the CH_4 conversion ratio (R_C) (Fig. 2), distributions of

251　the two chemical reaction rates (Fig. 3), and the distributions of gas species' molar fractions

11

252   (Fig. 4). The CH_4 conversion ratio is defined as the mole ratio of CH_4 over all carbon-contained

253   gas species at the outlet.

254   An important finding from Fig. 2 is that the conversion ratio of CH_4 increases significantly

255   with increasing pressure. This ratio is only 0.27 at 1 bar but is increased to about 0.7 at a

256   pressure of 2.7 bar. However, this ratio remains almost unchanged with further increase in

257   pressure. The CH_4 mole concentration at output, corresponding to the conversion ratio (Rc), is

258   increased from 1.26 to 16.38 mol/m^3 when the pressure is increased form 1 bar to 5 bar. With

259   the consideration of SOEC active area (0.775 cm^2), the CH_4 flow density, defined as volume

260   flux/ SOEC active area, also increases from 11.95 to 30.00 L/(min·m^2). This is because when

261   operating pressure is low, the CH_4 production is mainly dominated by the reversed MSR

262   enhanced by the increase of pressure (seen Fig. 3a). While at a high pressure, the influence of

263   CO concentration and H_2 concentration becomes significant for two reasons.

264   Firstly, the CO concentration and H_2 concentration are influenced by the WGSR, which

265   increases with increasing pressure. It can be seen from Fig. 3b that when the pressure is higher,

266   the reversed WGSR is increased in the SOEC section, which facilitates conversion of H_2 to CO.

267   This conversion in turn will limit the CH_4 production, as the exponential index of H_2 partial

268   pressure term is 3, while that of CO is 1 according to the equilibrium formula of MSR (Eq. 21).

269   Hence, the marginal benefit of pressure to the conversion ratio is reduced due to the enhanced

270   WGSR that converts too much H_2 to CO.

271   Secondly, the further increase of pressure will decrease the current density for co-electrolysis.

272   Since the simulated SOEC section is working under fixed voltage at 1.3 V, the equilibrium

273   potentials of H_2O (E_{H_2O}) and CO_2 (E_{CO_2}) electrolysis are increased by 0.03 and 0.1 volts with

274   increasing pressure to 5 bars, which means less overpotentials are allowed for the co-

275   electrolysis reactions. Thus the total electrolysis current slightly decreases as shown in Fig. 5.

276   As a result, less H_2 and CO are produced from the co-electrolysis reactions for CH_4 production

277   in the FT-like section.

278   The combined effect mentioned-above causes the maximum plateau value observed from the

279   CH_4 conversion ratio curve (Fig. 2).

280   Figure 3a shows the MSR rate distribution inside the cathode layer cut at 5 µm away from the

281   electrolyte-cathode interface. The MSR rates at the inlet are highly related to the operating

282   pressure since the rate expression for MSR is sensitive to gas partial pressures even though the

283   mole fraction are the same for all pressure values. When the pressure increases from 1 bar to 5

284   bar, the MSR rate at the inlet will changed from slightly positive (0.90 mol/(m^2·s)) to -28.01

285   mol/(m^2·s). When the flow streams forward, the MSR rate will converge to 0 quickly as the

286   gas mixture is approaching the equilibrium state. The gas composition is capable of self-

287   balancing quickly before the SOEC active region (the distance from the inlet: D = 1~1.6 cm).

288   However, for the 1 bar case, the MSR rate near the inlet is close to zero due to the low gas

289   partial pressure. The WGSR rate distribution at the same position is shown in Fig. 3b. When

290   increasing the operating pressure from 1 bar to 5 bar, the WGSR rate changed from -9.10

291   mol/(m^2·s) to -225.08 mol/(m^2·s). This is because the increased partial pressure of species in

292   reaction rate equation. Then the WGSR rate approaches 0 quickly, mainly due to the

293   consumption of CO_2. In the latter part of the SOEC section (D = 2 ~ 4 cm), The WGSR rate of

294   high operating pressure cases will be above that of low operating pressure. This is because the

295   generation of CH_4 due to via MSR reaction has consumed H_2 (product of WGSR) more than

296   CO (reactant of WGSR).

297   When the gas mixture enters the SOEC acitve region, the co-electrolysis of H_2O and CO_2

298   generates H_2 and CO, which can be clearly observed in H_2 and CO distribution in Fig. 4a and

299   4b. It should be mentioned that the mole amount of H_2O electrolyzed is much larger than that

300   of CO_2 (approximately 3.5 times) because the exchange current density of H_2O (i_{o,H_2O}=5300

301   Am^{-2}), is higher than that of CO_2 (i_{o,CO_2}=1590 Am^{-2}) used in this model [30], referred from

302   experimental investigations [34]. Therefore, the MSR rate drops to a certain negative value

303   (when D is between 1cm and 1.6cm) as shown in Fig. 3a inside the cathode layer, where the

304   H_2 and CO electrochemical sources exist.

305   It should be noted that this drop of MSR rate is only confined to be near the electrolyte-cathode

306   interface since the H_2 and CO sources are only significant at the region near this interface.

307   Figure 6 shows the distribution of MSR rate in the y direction, which is vertical to the flow

308   direction at D=1.4cm, which is caused by the fact that the co-electrolysis reactions only take

309   place in an limited active layer inside the electrode [35].

310   When the gas species enter the cooling zone where the temperature decreases from 800 ℃ to

311   250 ℃, the reversed MSR is activated significantly, e.g up to 32.5 mol/(m³·s) at 3 bar (Fig. 3).

312   This is simply bacause the decreasing of temperature will effectively change the equibilirim

313   state of MSR to the left side, favoring CH_4 production. The maxium rate of reversed MSR

314   reaction is reached at around 608 ℃, at D=5.3cm. However, a further decrease in temperture

315   will inhibit the reaction rate due to the Arrhenius law relationship between reaction rate and

316   temperature as specified in Eq. 24. In addition, the reversed MSR rate is also decreased as the

317   fuel gas is approaching equilibrium in the downstream of the reactor.

318   **3.2. Effects of temperature**

319   The temperature of the reactor significantly influences both the co-electrolysis in the SOEC

320   section and the chemical conversion inside the FT-like section. This part will focus on the

321   effects of operating temperature profile on the reactor performance. The unique design feature

322   of this reactor is the non-uniform temperature of the reactor, different from other reactors with

323   uniform working temperature [36,37]. In this SOEC-FT reactor, the SOEC section is at a high

324   temperature (i.e. 800 ℃) to facilitate the electrolysis reactions, while the FT-like section is

325   linearly decreased from the high temperature to a low temperature at the outlet to favor the

326   methanation reaction   [38, 39]. In the vertical direction, the temperature is assumed to be

327   uniform, since the diameter of the tubular reactor is only   about 0.4 cm.

328   To this end, the cooling gradient temperature settings employed in this paper creates a region

329   in the FT-like section which favors the reversed MSR. From this point of view, it is necessary

330   to optimize the temperature profile to improve the CH_4 sysnthsis by means of varying the

331   SOEC temperature and outlet temperature. The temperature profiles are shown in Table 2. The

332   simulated results are discussed below.

333   From Fig.7a it can be found that   the CH_4 output flux remains almost constant when the

334   temperature at the outlet of FT-like section (T_{FT}) is increased from 200 ℃ to 400 ℃. The CH_4

335   output flux within this temperature range is thus definded as the maximum CH_4 ouput flux

336   ($Q_{CH4.max}$), the value of which depends on the operating pressure. However, further increasing

337   T_{FT} will decrease the CH_4 output flux. This trend can be easily explained by the reduction of

338   equilbrium constant (Kpr) of MSR along the FT-like section. From the chemical model used

339   in this paper, the Kpr decreases expotentially when the temperature increases from 200 $^{\circ}$C to

340   800 ℃, thus the reversed MSR is not favored. This trend observed is also discussed in our

341   previous work [22]. Accordingly, a lower limit temperature of T_{FT} can be defined as $T_{FT, L}$.

342   When the T_{FT} is larger than this $T_{FT,L}$, the CH_4 output flux will be below 95% of the $Q_{CH4.max}$.

343   It is found from Fig. 7a that this lower-limit temperature varies with the operating pressure:

344   higher pressure leads to smaller value of the lower-limit temperature as shown in Fig. 8.

345   Therefore, the outlet temperature of FT-like section should be carefully maintained at a

346   relatively small value that allows for high CH_4 output, but still high enough to avoid destructive

347   thermal stress due to large temperature gradient.

348   Figure 7b gives the effects of the SOEC operating temperature on the CH$_4$ output flux.

349   Generally, as the T_{SOEC} increases from 600 to 1000 ℃, the CH$_4$ output improves, e.g. from 1.22

350   ml/min to 2.39 ml/min at 2 bar. It needs to mention that at high SOEC temperature (above

351   ca.900 ℃), the CH$_4$ ouput at 5 bar is smaller than that of 3 bar and close to the output at 2 bar.

352   Considering that the pressure effect on the CH$_4$ ouput is insignificant when the pressure is in

353   the range of 2-5 bar with T_{FT} at 250 ℃ as seen from Fig.7a, this decrease of CH$_4$ output from

354   3 to 5 bar, at 1000 ℃ should be ascribed to the decrease of electrolysis current while increasing

355   the pressure. In Fig. 9, the relationship between pressure and electrolysis current at $T_{SOEC} =$

356   1000 ℃ is shown to account for this trend.

3.3. Effects of electrolysis voltage

358   Electrolysis voltage is another important operating parameter for SOEC system, determing the

359   amount of electicity demand for H$_2$ and CO generation. Therefore, the CH$_4$ production of this

360   reactor is highly dependent on the operating voltage.

361   In this section, a parametric study of voltage at different pressure is conducted. As shown in

362   Fig. 10, the increase of voltage results in improvements of CH$_4$ output considerably. For

363   example, the CH$_4$ ouput can be doubled at 1 bar from 1.2 volt to 2.0 volt as 0.82 ml/min and

364   1.93 ml/min. Such trend remians in cases with higher pressure. At 2.0 volt and 5 bar, the

365   maxium CH$_4$ output reaches 2.97 ml/min. The mechanism for the positive effect of electrolysis

366   voltage is clear that higher voltage will lead to more H$_2$ and CO generation due to the higher

367   corresponding electrolysis current. The increase of H$_2$ and CO will facilitate the methane

368   production via reversed MSR reaction.

369   The current-voltage curves is also expected to be influenced by the pressure, as dipicted in Fig.

370   11. The comparison between curves at different pressures shows major factors that determine

371   the pressure effects on the current density. Firstly, at low voltage (< ca.1.5 volt), the increase

372 of pressure will result in small but observable decrease in the current density, ie 2530.2 to

373 2207.9 A/m^2. According to disscussion on the Nernst potential earlier in Fig. 5, it is reasonable

374 to attribute this decrease to the change of Nernst equibrilium potential. Unlikely, At high

375 voltage ie. 2.0 volt, an opposite trend is presented, which should be caused by the remarkably

376 changed gas species fraction condition when a high electrolysis voltage is applied. At high

377 voltage and high current, the concentration loss of the SOEC may play an important role. At

378 the same time, the increase of pressure can effectively enhance the H_2O amount in the SOEC

379 section by the enhanced reversed WGSR, so as to provide a more favorable species

380 concentration condition for the electrolysis reaction. This is the reason for the opposite trend

381 at high voltage when changing the pressure.

382 To verify this explanation, the ratio of H_2 to H_2O is given in Fig. 12. It can be seen that at 2.0

383 volt, the $\ln(x_{H_2}/x_{H_2O})$ term inside the cathode porous layer is much larger than that at 1.3V.

384 This means that the H_2O electrolysis is hard to proceed due to high fraction of products (i.e.

385 H_2) and low fraction of reactant (H_2O) at 2.0 volt. Then the increase of pressure can

386 significantly decrease the $\ln(x_{H_2}/x_{H_2O})$ term at 2.0 volt and the electrolysis process is easier

387 to take place. It is seen that the benefits from pressure increase is less significant at 1.3 volt,

388 mainly due to the lower current density for co-electrolysis and thus lower reaction rates of the

389 subsequent chemical reactions.

390 **3.4. Effects of exchange current density**

391 As mentioned, the exchange current densities for co-electrolysis reactions and oxygen

392 reduction reaction are crucial parameters as the activation overpotentials are sensitive to their

393 values especially at low current density condition [40]. Current endeavours of developing high

394 performance SOEC are focused on catalyst materials with higher catalytic activity [41, 42].

395 With the development of new electrode materials, it is highly possible to increase the exchange

396 current density at reduced temperature by a few times in comparison with the conventional

materials such as LSM. Hence in this study, the parametric studies of varying exchange

densities are carried out to evaluate the feasibility of the SOEC-FT reactor with better electrode

activity at reduced SOEC temperature.

As expected, reducing the temperature of the SOEC section from 800°C to 600°C considerably

decreases the co-electrolysis current density (Fig. 13a), which in turn decreases the CH_4

production (Fig. 13b).   However, with the exchange current density increased, the

electrochemical performance (current density for co-electrolysis) can be enhanced

substantially.   For instance, when increasing the exchange density by 3 times, the current

density is enhanced by about 1.58 times at 800 $^{\circ}$C and 1.49 times at 600 $^{\circ}$C (Fig. 13a).   As a

result, the CH_4 output can be compensated effectively by increasing the exchange current

density in case of lowering the working temperature (Fig. 13b).   In detail, for a reactor with

T_{SOEC} at 600°C, CH_4 output is increased by 27.17% when increasing the exchange current

density by 3 times at 3 bar, while only 8.47% at 800°C, 3 bar. This difference also applied to

all the operating pressures from 1 bar to 4 bar, indicating that pressurized SOEC-FT reactor

still have the room for CH_4 production improvement by using better electrodes. Generally, it

is more desirable to operate the SOEC at reduced temperature due to its merits such as: 1. wider

choices of lower cost materials, 2. lower operating cost, 3. reduction of manufacturing cost and

enhanced durability, though the efficiency of SOEC will be reduced to some extent at low

temperature. In view of this development trend, the temperature sensitivity study in this section

verified the feasibility of operating the SOEC-FT reactor at reduced temperature (i.e. 600°C)

without much CH_4 production drop in light of with further development in SOEC catalyst.

3.5. Discussion on energy perspectives

For the individual reactor unit, SOEC section is operated under a slightly endothermic mode when the operating voltage is 1.3 V and the co-electrolysis thermoneutral voltage is 1.359 V in most cases of this paper. That means a certain amount of heat (4.5% of electricity energy), should be supplied to generate H_2/CO rich fuel gas.

While for the FT-like section, much heat is designed to be released from the gas flow, which should be further recovered to heat up the inlet gas source from ambient temperature in a real system. The efficiency of this section would largely depend on the heat recovery system configuration (heat management, gas flux management) with the help of lots of auxiliary equipment such as heat exchanger, flow regulator, heater or cooler. And the post processing of the produced CH_4 rich outlet gas also plays a role in the unit efficiency. A general scheme for the post processing, in authors' perspective, should firstly be the separation of the methane content. Then the redundant H_2 and heat in the post-separation gas should be modulated with steam and small amount of H_2, recycled as the inlet gas. However, in this study, only the process inside the reactor is considered and the whole workflow cycle and heat management is beyond this paper's scope. Based on this understanding, the unit efficiency of the reactor is of less representative of the methanation system, thus not evaluated here.

4. Conclusion

A numerical electrochemical model is developed to analyse a pressurized SOEC-FT reactor for methane production. The effects of high operating pressure on the reactor performance are carefully evaluated. An optimal operating pressure for this reactor is predicted at around 3 bar, beyond which the CH_4 conversion ratio (2.5 times enhanced to 1 bar) cannot be further increased. The input electricity can also be reduced by lowering the electrolysis current density with higher pressure if voltage is constant. Pressure effects on co-electrolysis and methane steam reforming and water gas shift reactions are studied to understand the pressure effects on

444 the methanation process. Sensitivity studies of temperature and electrolysis voltage are

445 conducted to analyse the effects of this operating parameters on both the co-electrolysis and

446 methane synthesis. The prediction of CH_4 production using electrodes with higher exchange

447 current density shows that it is attractive to operate pressurized SOEC-FT reactor at low

448 temperature. Findings from the simulation results can be used to guide the optimization of the

449 SOEC-FT reactor such as the temperature settings, electrolysis voltage and operating pressure,

450 such parameters that determine the energy input, production rate, and reactor stability issues.

451 **Acknowledgement**

454

Nomenclature

Abbreviation

FT	Fischer Tropsch
SOEC	Solid oxide electrolysis cell
LSM	Lanthanum strontium manganite
YSZ	Yttrium stabilized zirconium
WGSR	Water gas shift reaction
MSR	Methane steam reforming reaction
FEM	Finite element method

Letters

i	Current density, $A \cdot m^{-2}$
σ	Conductivity for ion/electron, $\Omega^{-1} \cdot m^{-1}$
σ^{eff}	Effective conductivity for ion/electron, $\Omega^{-1} \cdot m^{-1}$
$\emptyset$	Potential, V
$Vcell$	Applied voltage, V
$V_{YSZ/LSM/Ni}$	Volume fraction of YSZ, LSM, or Ni phase
$\tau_{YSZ/LSM/Ni}$	Tortuosity factors
E	Equilibrium Nernst potential, V
η_{act}	Activation overpotential, V
η_{ohmic}	Ohmic overpotential, V
i_a, i_c	Local current source $A \cdot m^{-3}$
i_o	Exchange current density, $A \cdot m^{-2}$
AV_a, AV_c	Electrochemically active specific surface area, m^{-1}
R	Gas constant, 8.314 $J \cdot mol^{-1} \cdot K^{-1}$
R_c	CH$_4$ conversion ratio, the mole fraction of CH4 on
F	Faraday constant, 96485 $C \cdot mol^{-1}$
F_{vol}	Volume force, $N \cdot m^3$
p	(partial) Pressure, Pa
Q_{CH4}	CH$_4$ output flux, ml/min
R_{WGSR}	Reaction rate of water gas shift reaction, $mol \cdot m^{-3} \cdot s^{-1}$
R_{MSR}	Rate of methane steam reforming reaction, $mol \cdot m^{-3} \cdot s^{-1}$
U	Velocity field, $m^3 \cdot s^{-1}$
w_i	Mass fraction of species i
x_j	Mole fraction of species j
κ	Permeability, m^2
ε	Porosity
ρ	Fluid density, $kg \cdot m^{-3}$
μ	Dynamic viscosity of fluid, $Pa \cdot s$
D	Distance from the inlet, cm
D_{ij}	Binary diffusion coefficient of species i and j, $m^2 \cdot s^{-1}$
$D_{eff,ij}$	Effective binary diffusion coefficient of i and j, $m^2 \cdot s^{-1}$
$D_{k, i}$	Knudsen diffusion coefficient of i , $m^2 \cdot s^{-1}$
S_m	Mass source term, $kg \cdot m^{-3} \cdot s^{-1}$
S_i	Mass source term of species i due to electrolysis, $kg \cdot m^{-3} \cdot s^{-1}$
R_i	Mass source term of species i due to chemical reaction, $kg \cdot m^{-3} \cdot s^{-1}$

r_e	Average radius of pores, m
T_{SOEC}	Temperature of SOEC section, ℃
T_{FT}	Temperature of outlet at FT section, ℃
K_{pr}, K_{ps}	Equilibrium constant of MSR and WGSR

460

461

Reference

[1] Wendel CH, Braun RJ. Design and techno-economic analysis of high efficiency reversible solid oxide cell systems for distributed energy storage. Applied Energy. 2016;172:118-31.

[2] Jensen SH, Sun XF, Ebbesen SD, Knibbe R, Mogensen M. Hydrogen and synthetic fuel production using pressurized solid oxide electrolysis cells. International Journal of Hydrogen Energy. 2010;35:9544-9.

[3] Ni M. 2D thermal modeling of a solid oxide electrolyzer cell (SOEC) for syngas production by H2O/CO2 co-electrolysis. International Journal of Hydrogen Energy. 2012;37:6389-99.

[4] Wendel CH, Gao Z, Barnett SA, Braun RJ. Modeling and experimental performance of an intermediate temperature reversible solid oxide cell for high-efficiency, distributed-scale electrical energy storage. Journal of Power Sources. 2015;283:329-42.

[5] Zhang H, Wang J, Su S, Chen J. Electrochemical performance characteristics and optimum design strategies of a solid oxide electrolysis cell system for carbon dioxide reduction. International Journal of Hydrogen Energy. 2013;38:9609-18.

[6] Wei FB, Dao MM, Song PY, Lu XM, Zhang HC, Zhang JJ, et al. Evaluation on the Efficiency of a Solar Powered Solid Oxide Electrolysis Cell Plant for Carbon Dioxide Reduction. Int J Electrochem Soc. 2014;9:1146-62.

[7] Li WY, Wang HJ, Shi YX, Cai NS. Performance and methane production characteristics of H2O-CO2 co-electrolysis in solid oxide electrolysis cells. International Journal of Hydrogen Energy. 2013;38:11104-9.

[8] Hansen JB. Process for converting biogas to a gas rich in methane. Google Patents; 2014.

[9] Stempien JP, Ni M, Sun Q, Chan SH. Thermodynamic analysis of combined Solid Oxide Electrolyzer and Fischer–Tropsch processes. Energy. 2015;81:682-90.

[10] Schlitzberger C, Brinkmeier NO, Leithner R. CO2 Capture in SOFC by Vapor Condensation and CH4 Production in SOEC Storing Excess Electricity. Chemical Engineering & Technology. 2012;35:440-4.

[11] Kato T, Nagata S, Honda T, Negishi A, Tanaka Y, Momma A. Possibility of Methane Production from Steam and Carbon Dioxide by Using Solid Oxide Electrolysis Cells. Ecs Transactions. 2015;68:3513-8.

[12] Wendel C, Braun R. Thermodynamic considerations for a novel solid oxide flow battery system for grid-energy storage. equilibrium.2:10.

[13] Botta G, Solimeo M, Leone P, Aravind P. Thermodynamic Analysis of Coupling a SOEC in Co-Electrolysis Mode with the Dimethyl Ether Synthesis. Fuel Cells. 2015;15:669-81.

[14] Penchini D, Cinti G, Discepoli G, Desideri U. Theoretical study and performance evaluation of hydrogen production by 200 W solid oxide electrolyzer stack. International Journal of Hydrogen Energy. 2014;39:9457-66.

[15] Buonomano A, Calise F, d'Accadia MD, Palombo A, Vicidomini M. Hybrid solid oxide fuel cells–gas turbine systems for combined heat and power: A review. Applied Energy. 2015;156:32-85.

[16] Boerrigter H, Rauch R. Review of applications of gases from biomass gasification. ECN Biomassa, Kolen en Milieuonderzoek. 2006;20.

[17] Becker WL, Braun RJ, Penev M, Melaina M. Production of Fischer–Tropsch liquid fuels from high temperature solid oxide co-electrolysis units. Energy. 2012;47:99-115.

[18] Wilhelm DJ, Simbeck DR, Karp AD, Dickenson RL. Syngas production for gas-to-liquids applications: technologies, issues and outlook. Fuel Process Technol. 2001;71:139-48.

[19] Jager B, Espinoza R. Advances in low temperature Fischer-Tropsch synthesis. Catal Today. 1995;23:17-28.

[20] Cinti G, Baldinelli A, Di Michele A, Desideri U. Integration of Solid Oxide Electrolyzer and Fischer-Tropsch: A sustainable pathway for synthetic fuel. Applied Energy. 2016;162:308-20.

[21] Chen L, Chen FL, Xia CR. Direct synthesis of methane from CO_2-H_2O co-electrolysis in tubular solid oxide electrolysis cells. Energ Environ Sci. 2014;7:4018-22.

[22] Chen B, Xu H, Chen L, Li Y, Xia C, Ni M. Modelling of One-Step Methanation Process Combining SOECs and Fischer-Tropsch-like Reactor. Journal of The Electrochemical Society. 2016;163:F3001-F3008.

[23] Sun X, Chen M, Jensen SH, Ebbesen SD, Graves C, Mogensen M. Thermodynamic analysis of synthetic hydrocarbon fuel production in pressurized solid oxide electrolysis cells. International Journal of Hydrogen Energy. 2012;37:17101-10.

[24] Henke M, Willich C, Kallo J, Friedrich KA. Theoretical study on pressurized operation of solid oxide electrolysis cells. International Journal Of Hydrogen Energy. 2014;39:12434-9.

[25] Amestoy PR, Duff IS, L'Excellent J-Y. Multifrontal parallel distributed symmetric and unsymmetric solvers. Comput Method Appl M. 2000;184:501-20.

[26] Ni M, Leung MKH, Leung DYC. Mathematical Modelling of Proton-Conducting Solid Oxide Fuel Cells and Comparison with Oxygen-Ion-Conducting Counterpart. Fuel Cells. 2007;7:269-278.

[27] Chan SH, Khor KA, Xia ZT. A complete polarization model of a solid oxide fuel cell and its sensitivity to the change of cell component thickness. Journal of Power Sources. 2001;93:130-40.

[28] Van Der Laan GP, Beenackers A. Kinetics and selectivity of the Fischer–Tropsch synthesis: a literature review. Catalysis Reviews. 1999;41:255-318.

[29] Haberman BA, Young JB. Three-dimensional simulation of chemically reacting gas flows in the porous support structure of an integrated-planar solid oxide fuel cell. International Journal of Heat and Mass Transfer. 2004;47:3617-29.

[30] Ni M. Modeling and parametric simulations of solid oxide fuel cells with methane carbon dioxide reforming. Energy Conversion and Management. 2013;70:116-129.

[31] Whitaker S. Diffusion and dispersion in porous media. AIChE Journal. 1967;13:420-7.

[32] Mason EA, Malinauskas A. Gas transport in porous media: the dusty-gas model: Elsevier Science Ltd; 1983.

[33] Sun XF, Chen M, Jensen SH, Ebbesen SD, Graves C, Mogensen M. Thermodynamic analysis of synthetic hydrocarbon fuel production in pressurized solid oxide electrolysis cells. International Journal Of Hydrogen Energy. 2012;37:17101-10.

[34] Matsuzaki Y, Yasuda I. Electrochemical Oxidation of H 2 and CO in a H 2-H 2 O-CO-CO 2 System at the Interface of a Ni-YSZ Cermet Electrode and YSZ Electrolyte. Journal of the Electrochemical Society. 2000;147:1630-5.

[35] Zheng K, Li L, Ni M. Investigation of the electrochemical active thickness of solid oxide fuel cell anode. International journal of hydrogen energy. 2014;39:12904-12.

[36] Ni M. An electrochemical model for syngas production by co-electrolysis of H_2O and CO_2. Journal of Power Sources. 2012;202:209-216.

[37] Bierschenk DM, Wilson JR, Barnett SA. High efficiency electrical energy storage using a methane-oxygen solid oxide cell. Energ Environ Sci. 2011;4:944-51.

[38] Ni M. Modeling of SOFC running on partially pre-reformed gas mixture. International Journal of Hydrogen Energy. 2012; 37(2): 1731-1745.

[39] Choudhary VR, Rajput AM, Prabhakar B. Nonequilibrium Oxidative Conversion of Methane to CO and H2 with High Selectivity and Productivity over Ni/Al2O3 at Low Temperatures. J Catal. 1993;139:326-8.

[40] Ni M, Leung MKH, Leung DYC. Parametric study of solid oxide fuel cell performance. Energy Conversion and Management. 2007;48:1525-35.

560 [41] Dong F, Ni M, He W, Chen Y, Yang G, Chen D, et al. An efficient electrocatalyst as
561 cathode material for solid oxide fuel cells: BaFe 0· 95 Sn 0· 05 O 3− δ. Journal of Power
562 Sources. 2016;326:459-65.
563 [42] Dong F, Ni M, Chen Y, Chen D, Tadé MO, Shao Z. Structural and oxygen-transport
564 studies of double perovskites PrBa 1− x Co 2 O 5+ δ (x= 0.00, 0.05, and 0.10) toward their
565 application as superior oxygen reduction electrodes. Journal of Materials Chemistry A.
566 2014;2:20520-9.

567

568

Table 1. Structural and operating parameters of cell [11]

Parameters	Value
Cell length (cm)	8
Inner diameter (cm)	0.35
Cathode thickness (μm)	308
Anode thickness (μm)	30
Electrolyte thickness (μm)	12
FT section length (cm)	4.2
Outlet temperature of FT Section, T_{FT} (ºC)	250 (base case)
Temperature of SOEC, T_{SOEC} (ºC)	800 (base case)
Operating pressure (bar)	1.0~5.0
Porosity, ε	0.55
Tortuosity, ξ	2.5
Permeability of the porous layer, κ	1.76
Voltage, V_{cell} (V)	1.3; 1.5
Inlet gas flux (SCCM)	18.9
Inlet gas composition	
Fuel: H_2:CO_2 (20%vol H_2O)	3.566 [22]
Air: O_2:N_2	0.21:0.79

Table 2. Settings for sensitivity studies

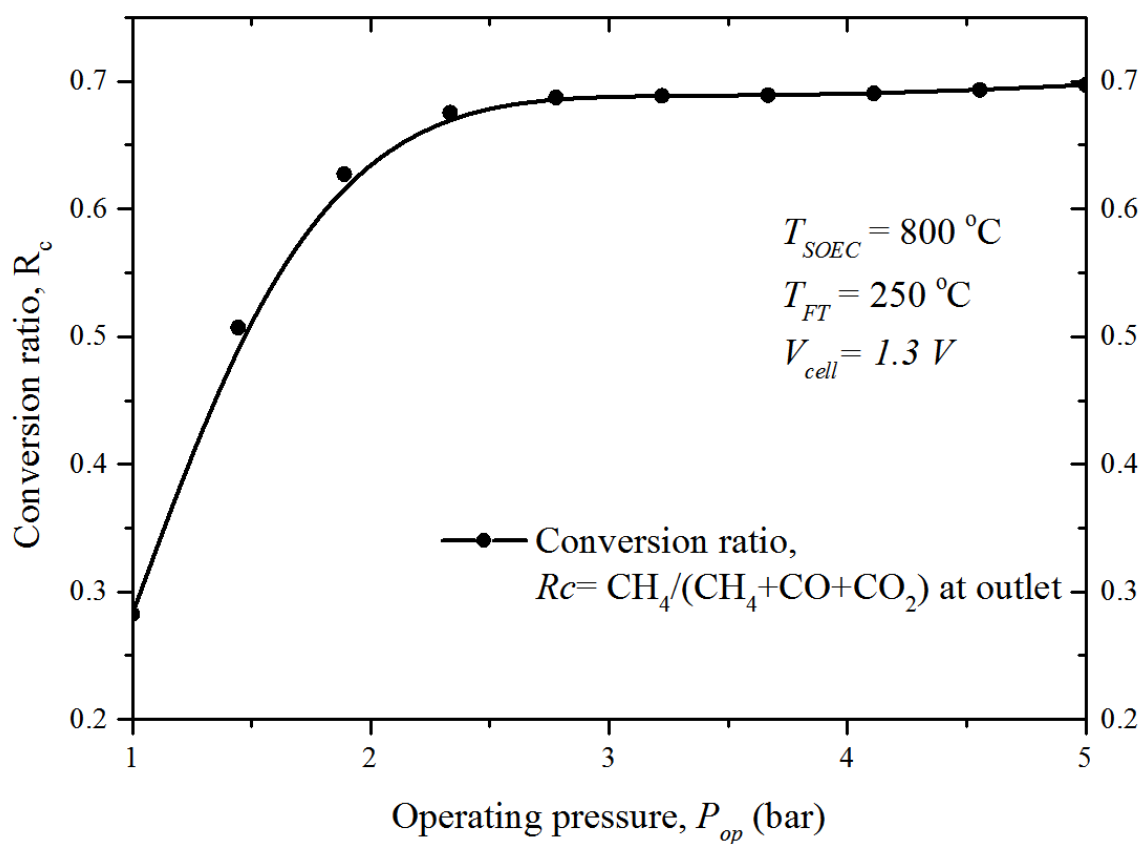| Sensitivity study case	Pressure (bar)	Temperature		Voltage (V)	Exchange current density (A m^{-2})
		SOEC section temperature, T_{SOFC} (ºC)	Outlet temperature of FT-like section, T_{FT} (ºC)		
Basic case	1	800	250	1.3	i_o
1. Pressure	1~5	800	250	1.3	i_o
2. Temperature	1~5	800 600~1000	200~800 250	1.3	i_o
3. Voltage	1~5	800	250	1.2~2.0	i_o
4. Exchange current density	1~5	800	250	1.3	i_o~ $3i_o$

579 List of Figures

580

581 Fig. 1. Schematic of SOEC-FT reactor

582 Fig. 2. CH_4 conversion ratio vs. Operating pressure at the reactor's outlet
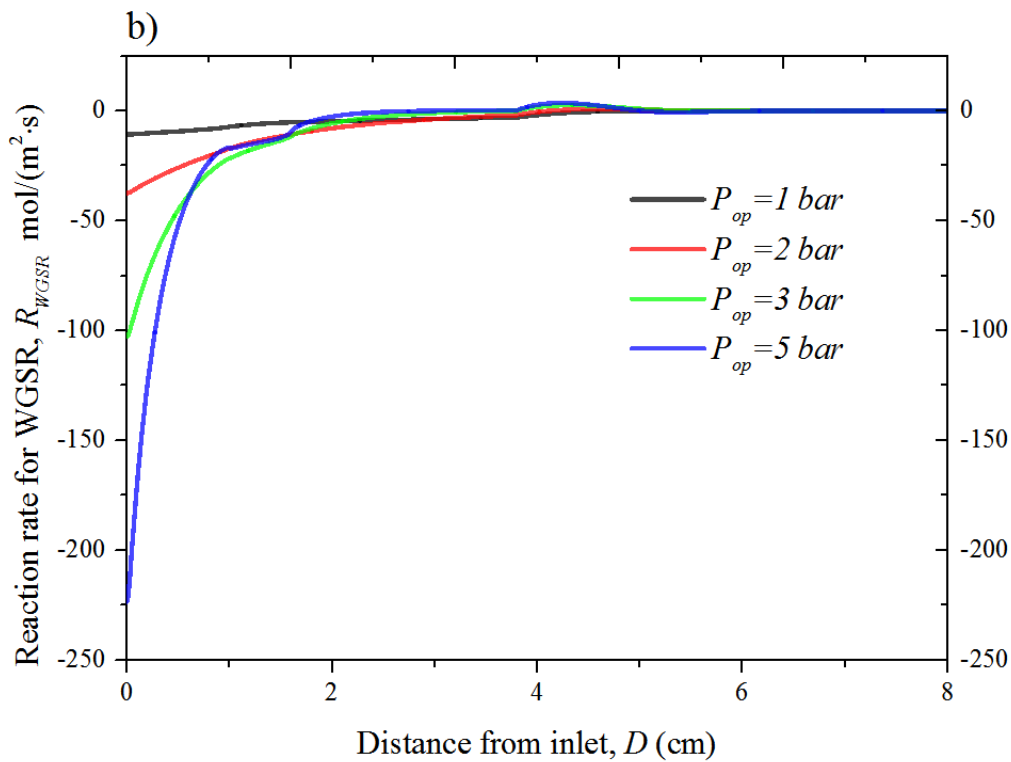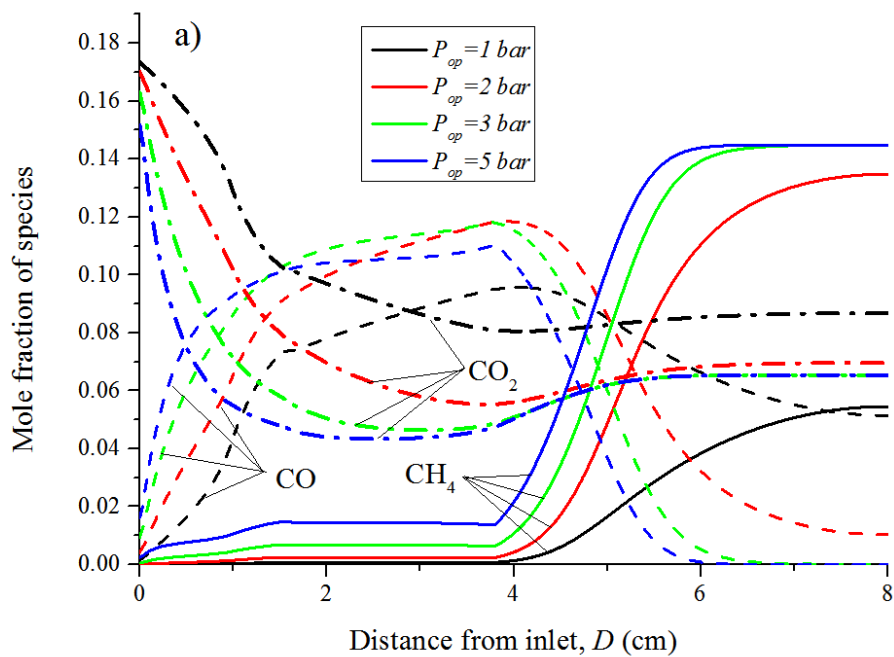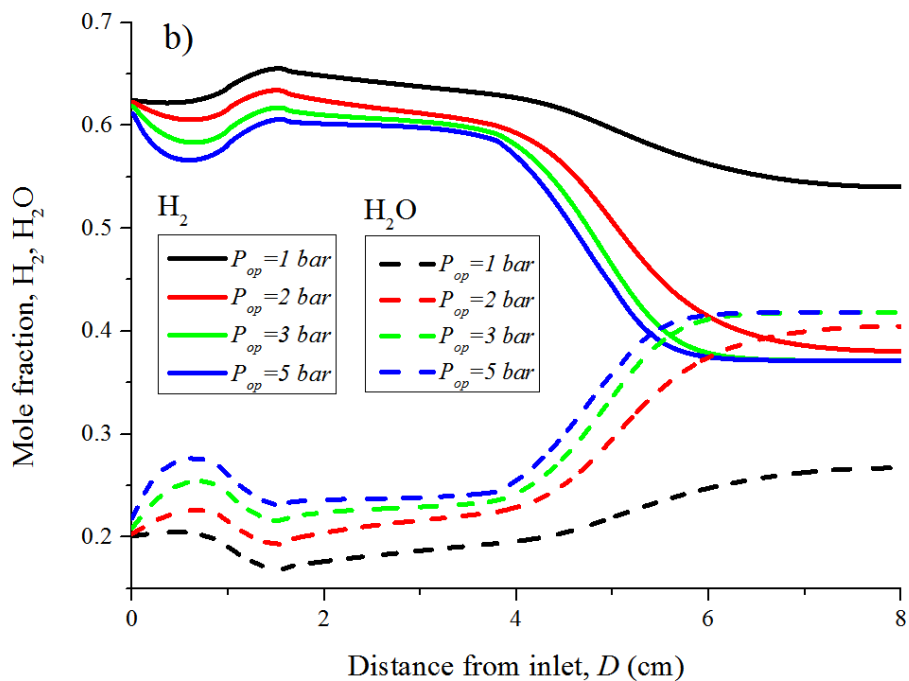
583 Fig. 3. a) Distribution of MSR rate along the flow direction, b) Distribution of WGSR rate
584 along the flow direction

585 Fig. 4. a) CH_4, CO and CO_2 mole fraction distribution along the flow direction, b) H_2 and H_2O
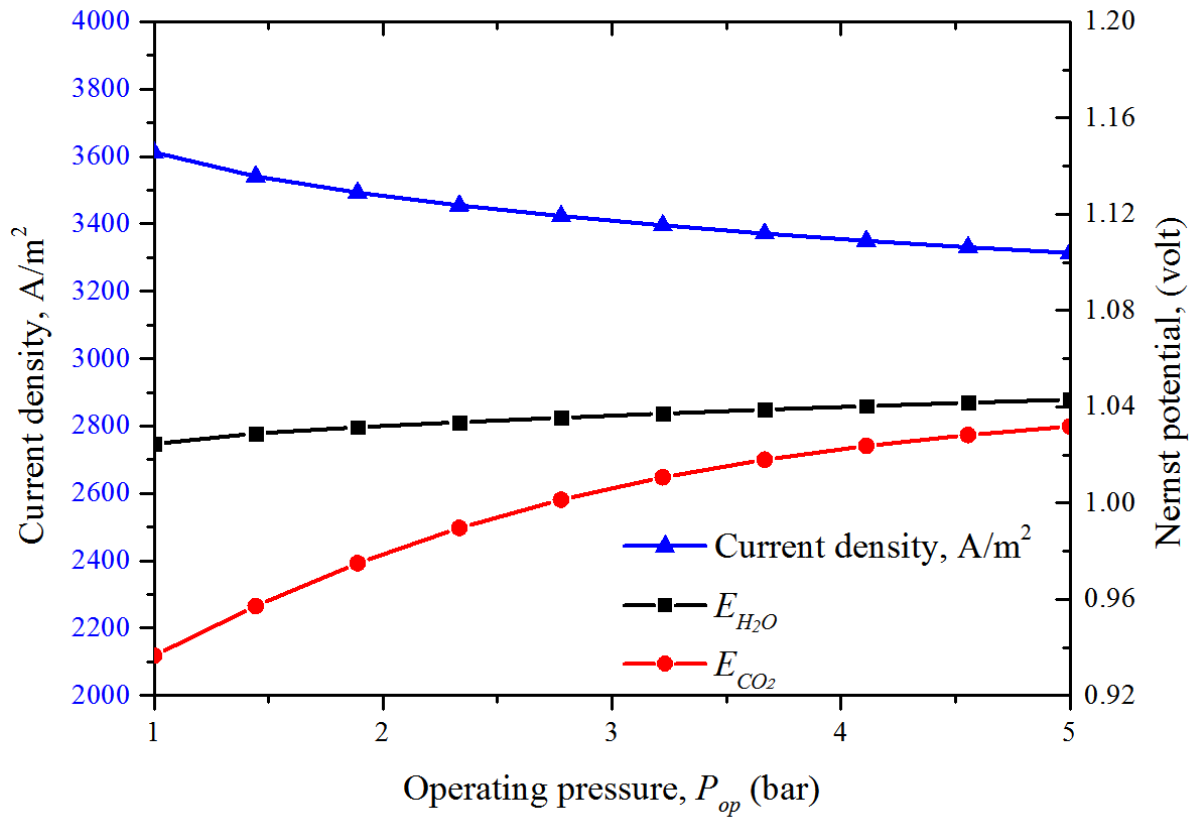586 mole fraction along the flow direction

587 Fig. 5 Effects of the pressure on the co-electrolysis current density, and equilibrium Nernst
588 potentials (E_{H_2O} and E_{CO_2})

589 Fig. 6 MSR rate distribution in y direction (vertical to the flow direction)

590 Fig. 7. a) CH_4 output flux vs. outlet temperature of the FT section (T_{FT}), with T_{SOEC} at 800 ℃,
591 b) CH_4 output flux vs. SOEC section temperature (T_{SOEC}) with T_{FT} at 250 ℃

592 Fig. 8. The effects of operating pressure on lower limit temperature ($T_{FT, L}$) when 95%
593 maximum CH_4 achieved

594 Fig. 9. Current density vs. Operating pressure (P_{op}) at T_{SOEC} = 1000 ℃ and T_{FT} = 250 ℃

595 Fig. 10. The effects of electrolysis voltage (1.2-2.0 volt) on the CH_4 output flux (ml/min) when
596 changing the operating pressure (1-5 bar)

597 Fig. 11. I-V curves for SOEC-FT reacotor at different operating pressure (1-5 bar)

598 Fig. 12. The nature logarithm of the ratio of H_2 mole fraction to H_2O mole fraction noted as
599 $\ln(x_{H_2}/x_{H_2O})$ along the flow direction, 5 um close to the electrolyte-cathode interface, at
600 different voltage (1.3 volt and 2.0 volt) and operating pressure (1-5 bar)

601 Fig. 13 a) The current density of SOEC-FT reactor at 800 ℃ and 600 ℃ with exchange current
602 density increased from i_o to $3i_o$, b) The CH_4 outlet flux at 800 ℃ and 600 ℃ with exchange
603 current density increased from i_o to $3i_o$

604

605

27

606   Figure 1

SOEC Section (T=800 ºC)   Air   F-T Section (T=800 ºC to 250 ºC)

O_2

$CO_2/H_2O/H_2$ H_2O H_2 CO_2 CO $3H_2+CO$ CH_4+H_2O Fuel Outlet r

H_2+CO2 $CO+H_2O$

Cathode layer

Anode layer   Electrolyte
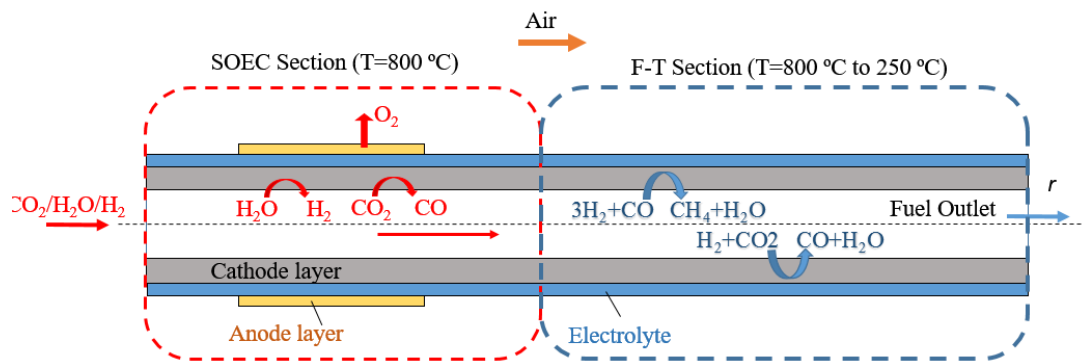
607

608   Fig. 1. Schematic of SOEC-FT reactor

609

610   Figure 2

611
612

$T_{SOEC} = 800\ ^{o}C$

$T_{FT} = 250\ ^{o}C$

$V_{cell} = 1.3\ V$

Conversion ratio,
$Rc = CH_4/(CH_4+CO+CO_2)$ at outlet

613
614   Fig. 2. CH_4 conversion ratio vs. Operating pressure at the reactor's outlet

615
616

617   Figure 3

a)

618

b)
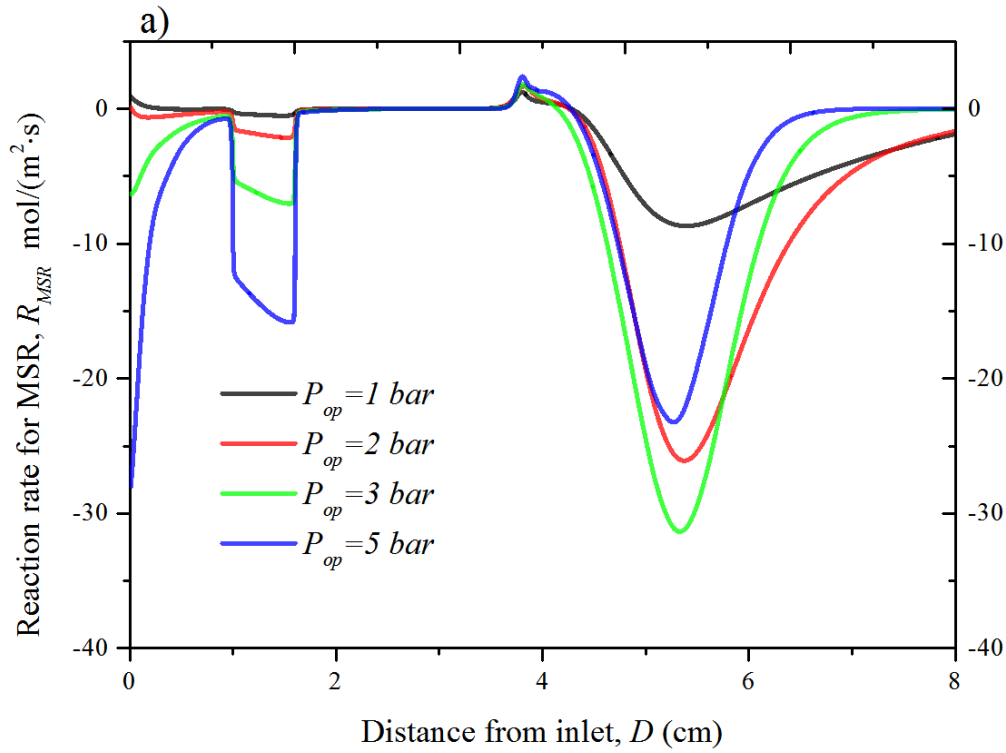
619

620   Fig. 3. a) Distribution of MSR rate along the flow direction, b) Distribution of WGSR rate
621   along the flow direction

622

623   Figure 4

624

625

626

Fig. 4. a) CH_4, CO and CO_2 mole fraction distribution along the flow direction, b) H_2 and
H_2O mole fraction along the flow direction

629

630

631

632

633   Figure 5

634

635   Fig. 5 Effects of the pressure on the co-electrolysis current density, and equilibrium Nernst
636   potentials (E_{H_2O} and E_{CO_2})

637

638   Figure 6

639
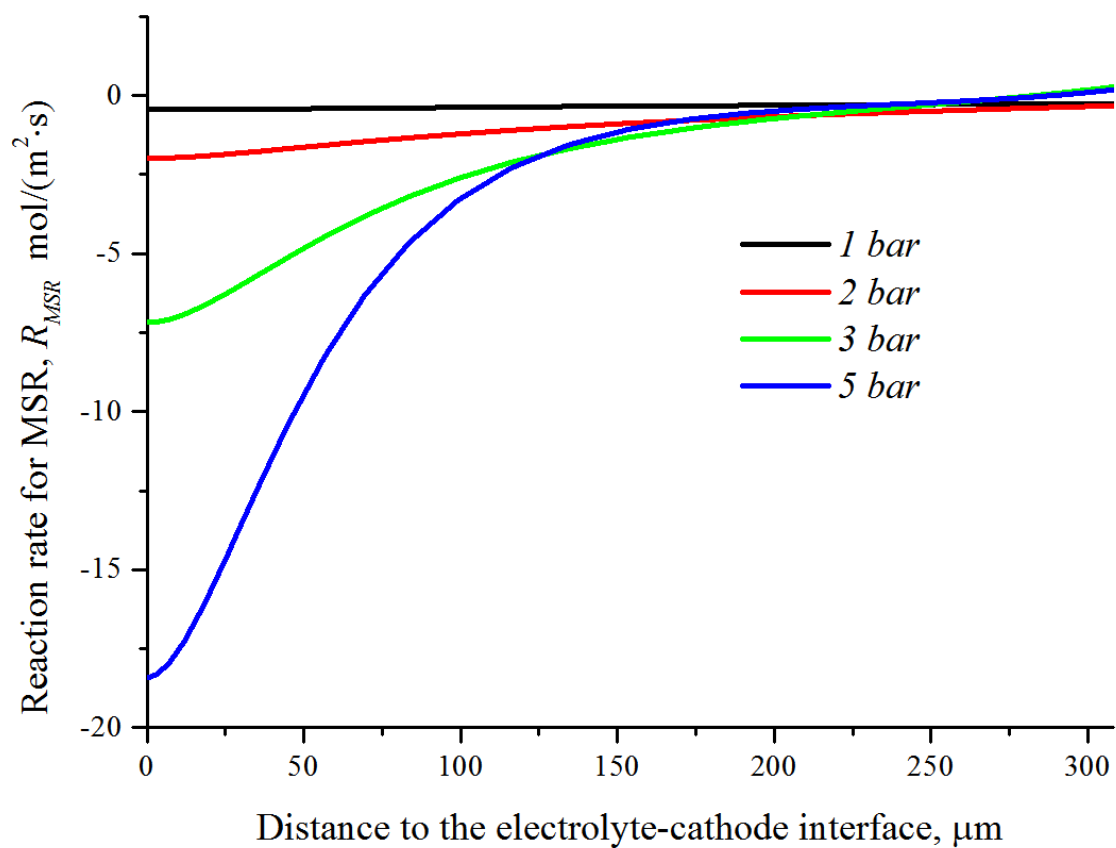
640

641   Fig. 6 MSR rate distribution in y direction (vertical to the flow direction)

642
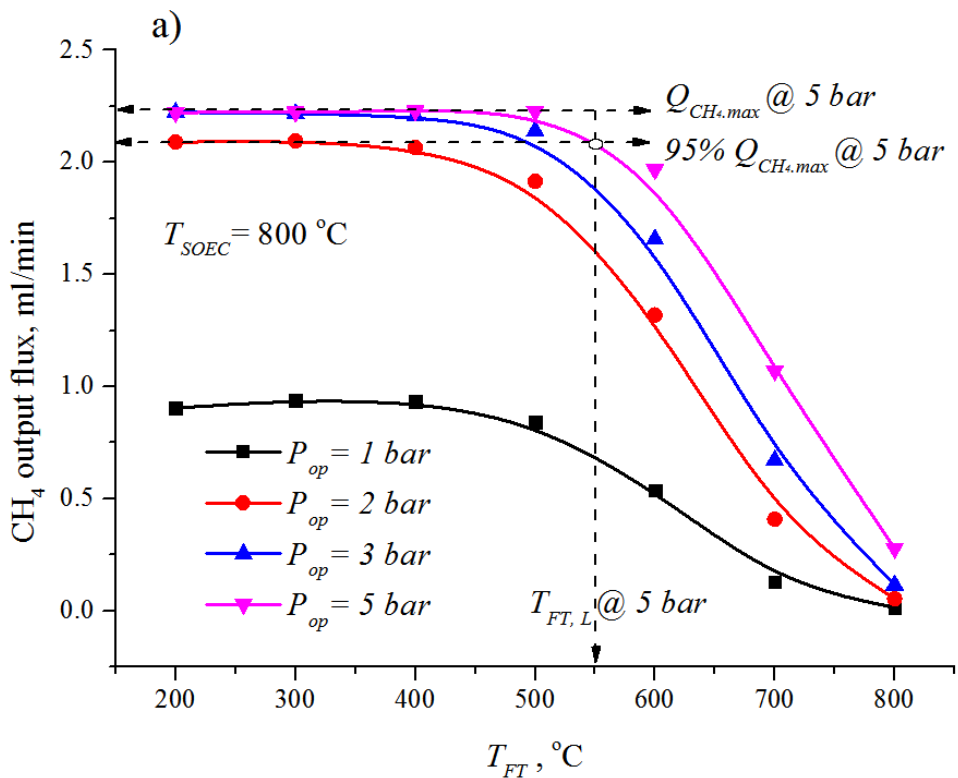
643   Figure 7
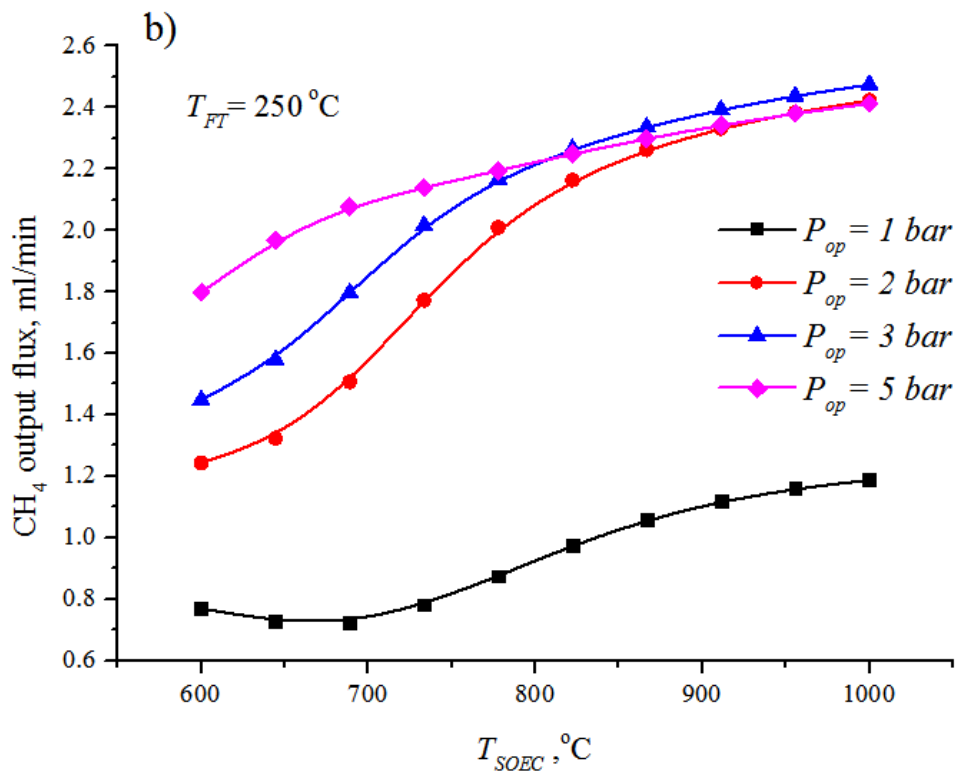
Fig. 7. a) CH$_4$ output flux vs. outlet temperature of the FT section (T_{FT}), with T_{SOEC} at 800 ℃,
b) CH$_4$ output flux vs. SOEC section temperature (T_{SOEC}) with T_{FT} at 250 ℃

649　Figure 8

$T_{SOEC} = 800\ ^{\circ}\text{C}$

$Q_{CH_4} < 95\%\ Q_{CH_4,max}$, if $T_{FT} > T_{FT,L}$

Lower limit temperature, $T_{FT,L}$ (°C)

534

488

455

444

Operating pressure, P_{op} (bar)
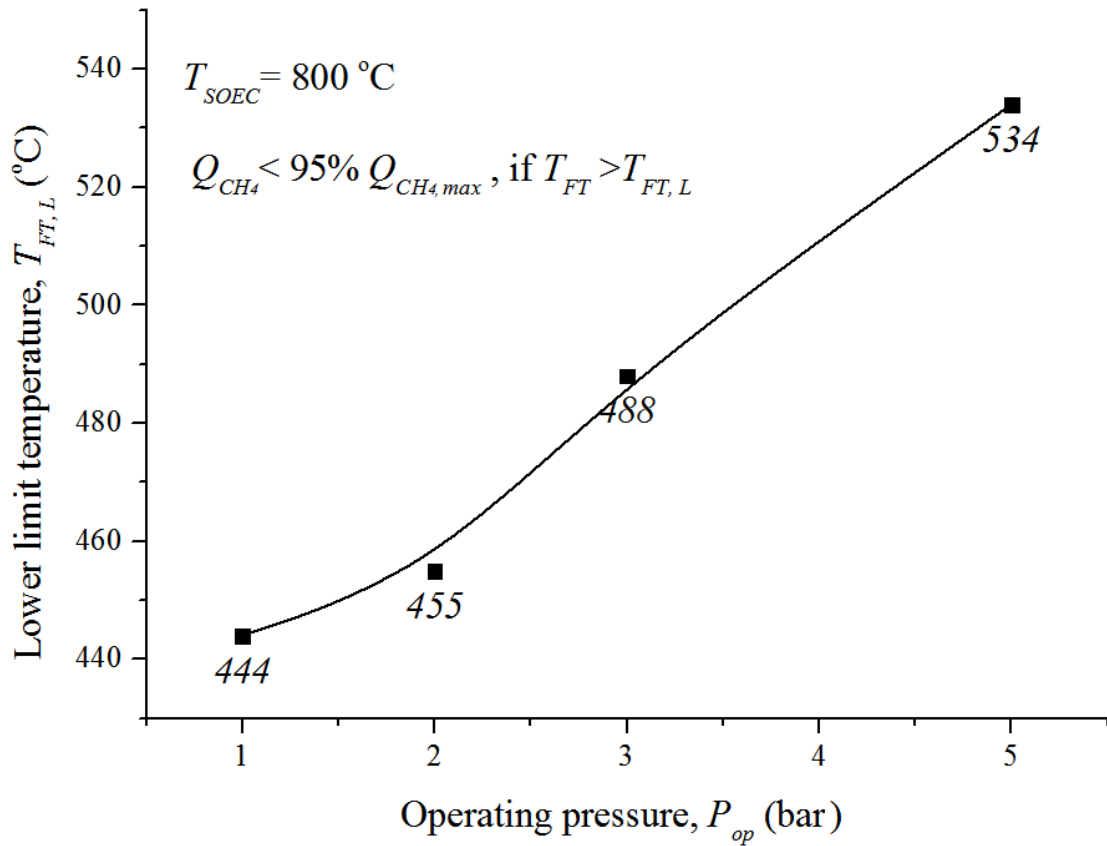
650

651　Fig. 8. The effects of operating pressure on lower limit temperature ($T_{FT,L}$) when 95%
652　maximum CH_4 achieved

653

654   Figure 9
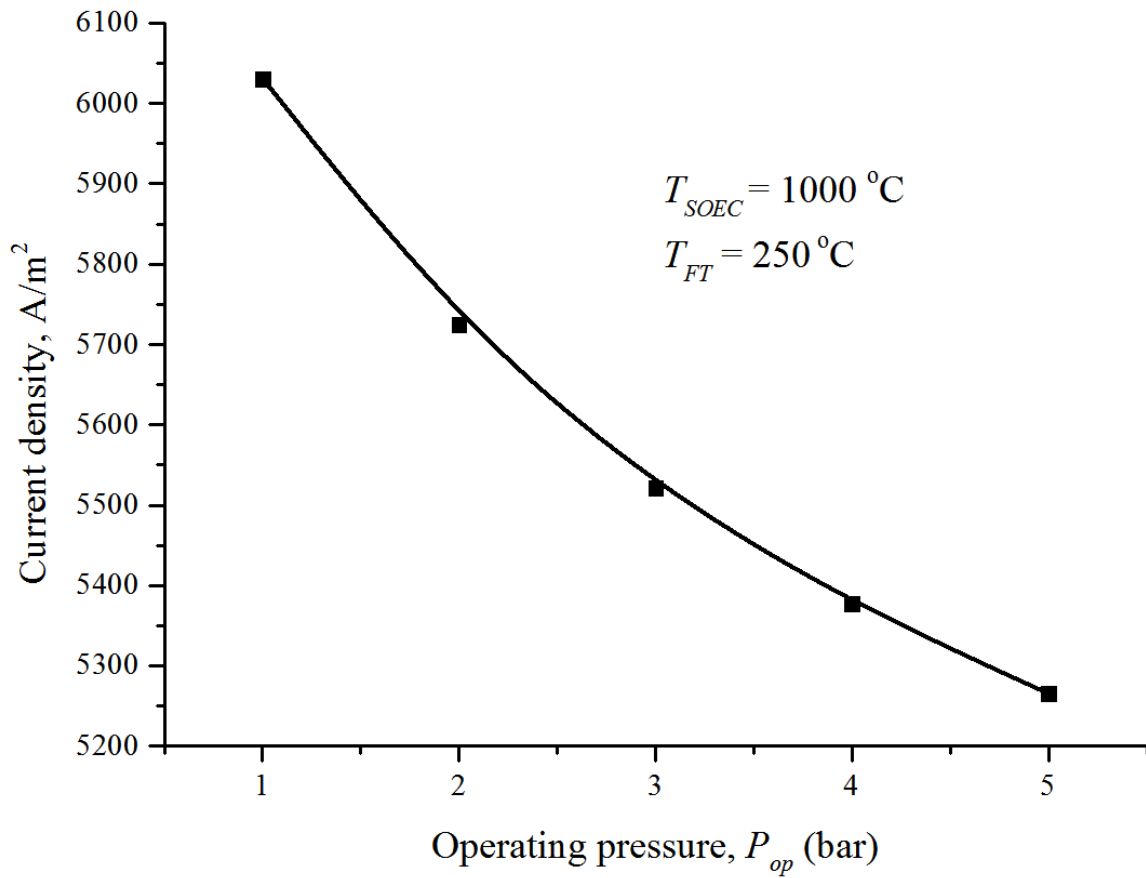
655

656   Fig. 9. Current density vs. Operating pressure (P_{op}) at T_{SOEC} = 1000 °C and T_{FT} = 250 °C

657

658

659

660   Figure 10
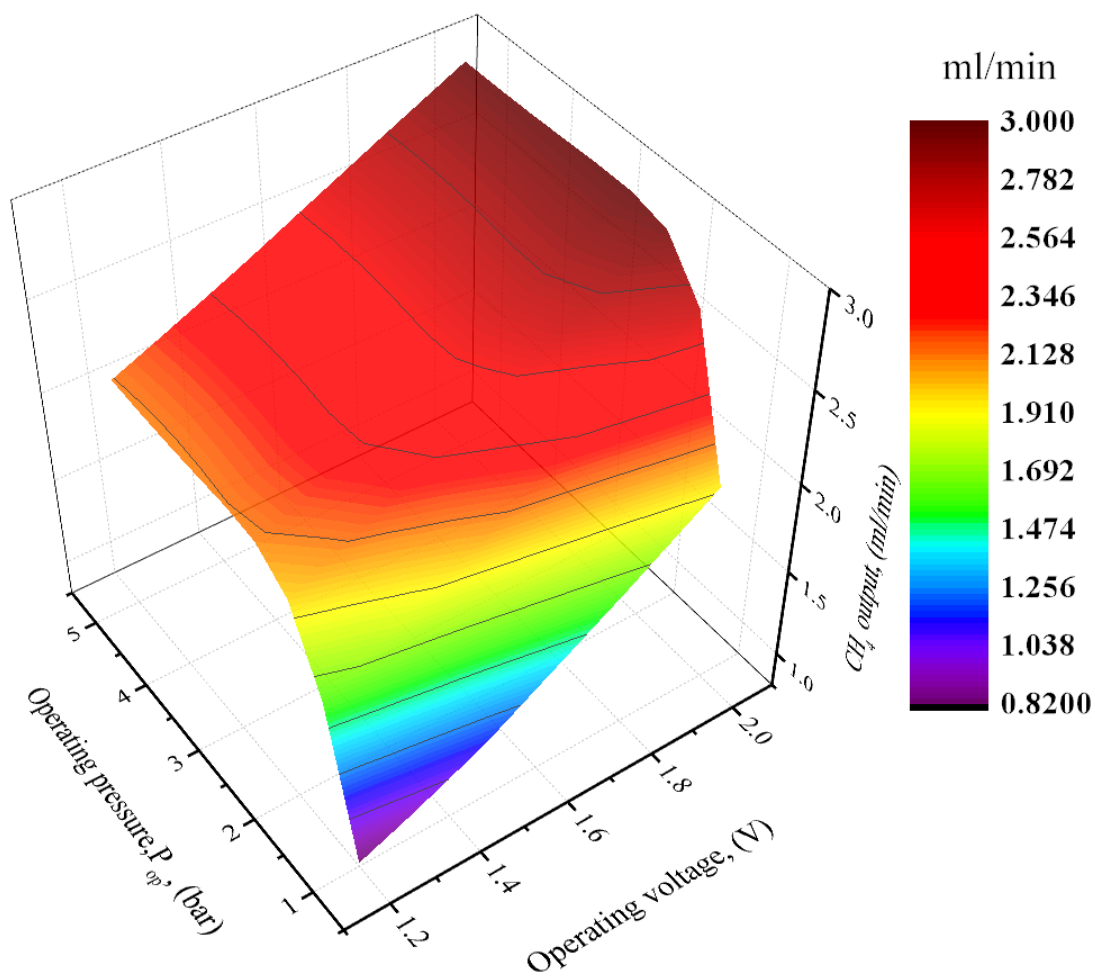
661

662   Fig. 10. The effects of electrolysis voltage (1.2-2.0 volt) on the CH_4 output flux (ml/min)
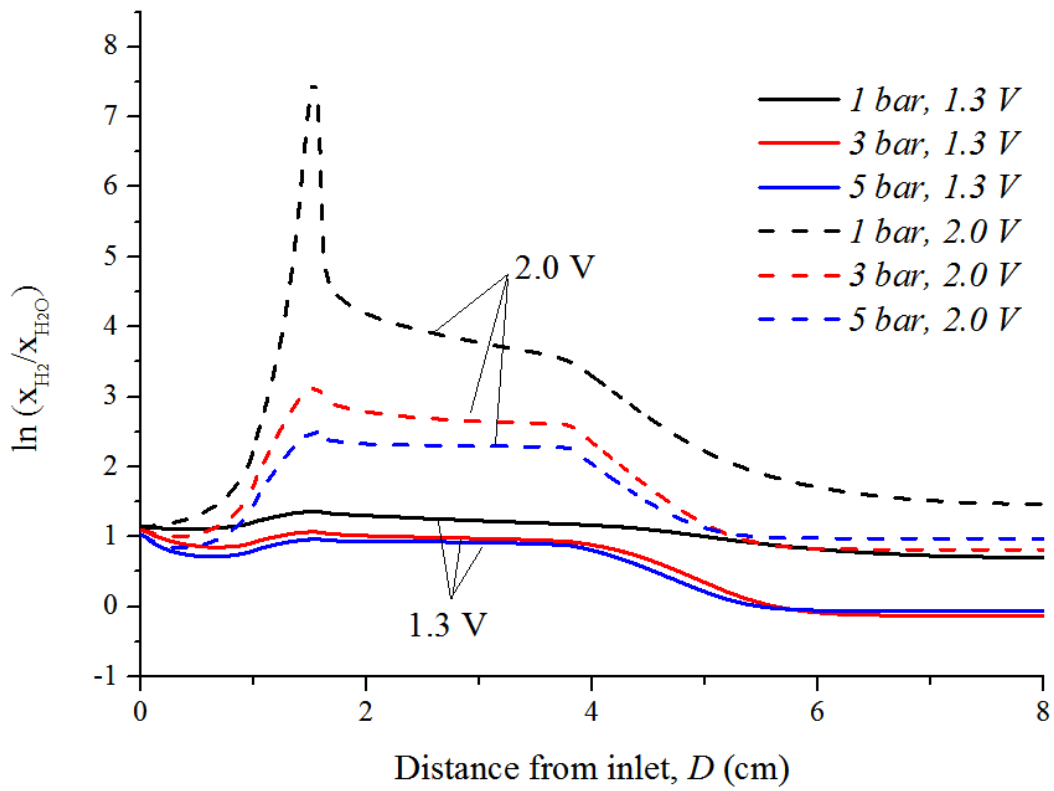663   when changing the operating pressure (1-5 bar)

664

665   Figure 11
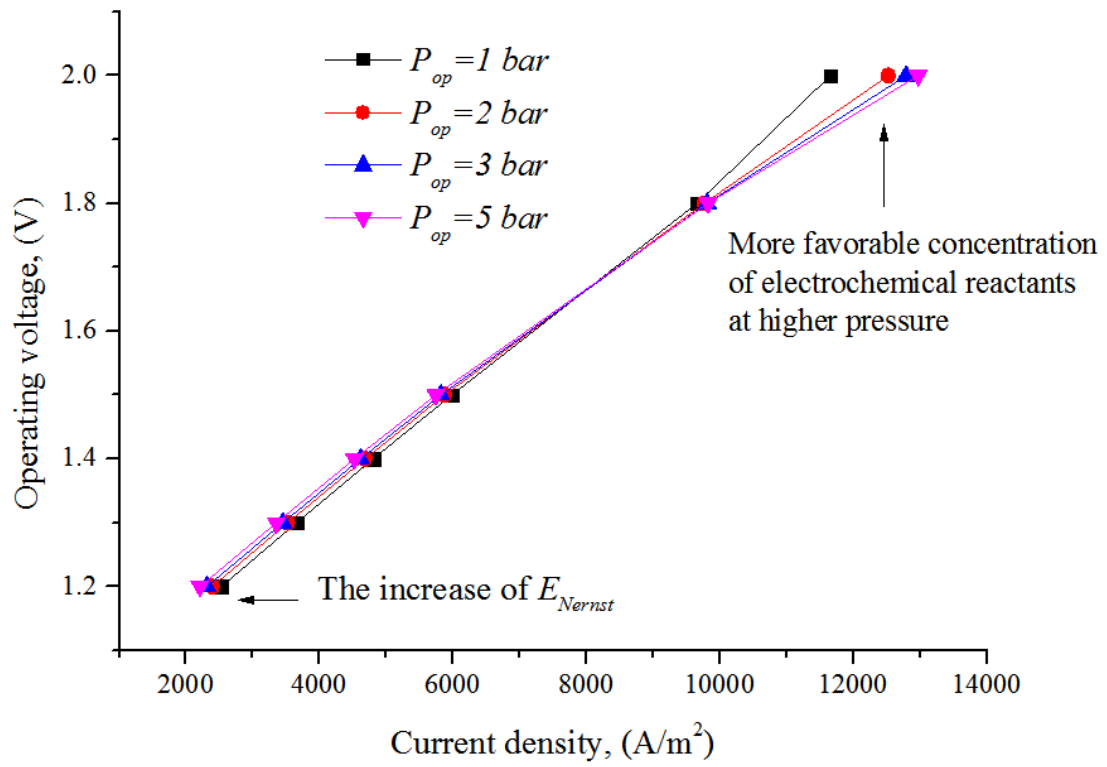
666

667

668   Fig. 11. I-V curves for SOEC-FT reactor at different operating pressure (1-5 bar)
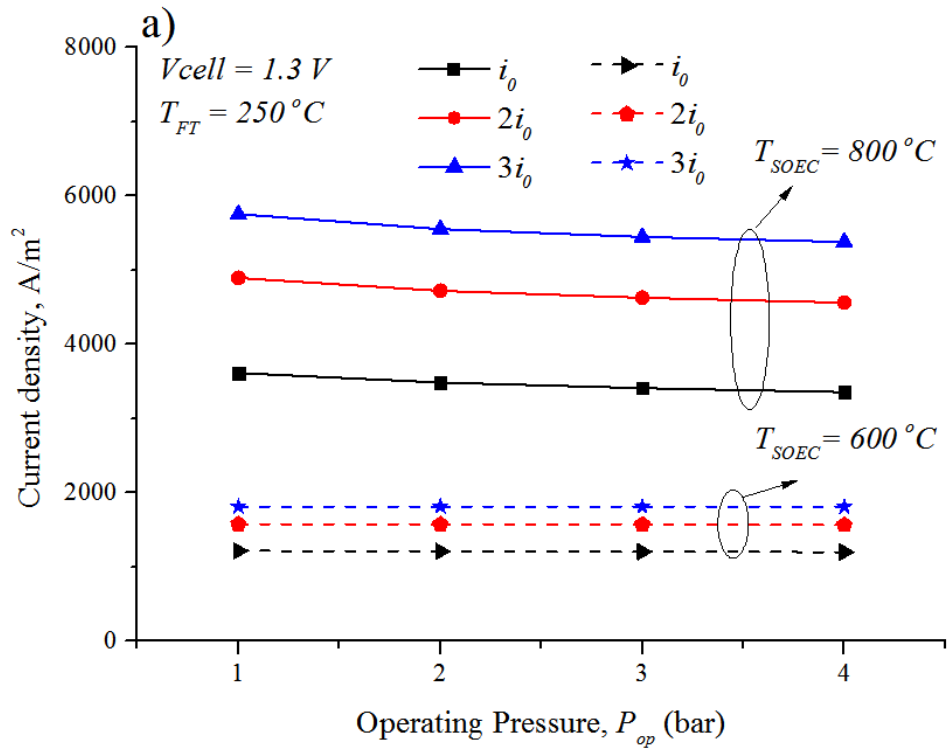
669

670

671   Figure 12

672

673
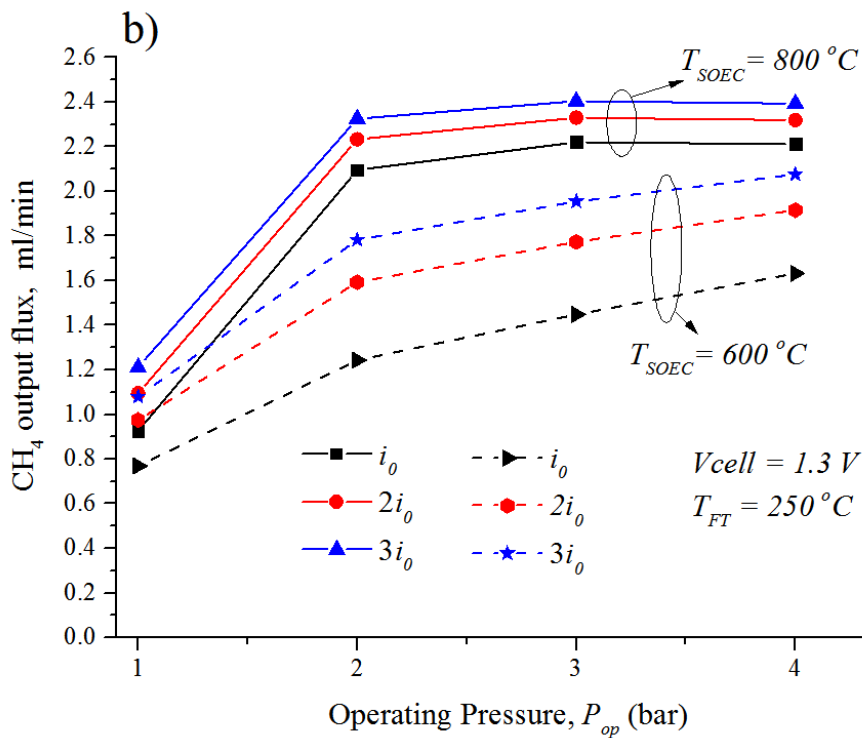674   Fig. 12. The nature logarithm of the ratio of H$_2$ mole fraction to H$_2$O mole fraction noted as
675    $\ln(x_{H_2}/x_{H_2O})$ along the flow direction, 5 um close to the electrolyte-cathode interface, at
676   different voltage (1.3 volt and 2.0 volt) and operating pressure (1-5 bar)

677

678   Figure 13

680

681   Fig. 13 a) The current density of SOEC-FT reactor at 800 ℃ and 600 ℃ with exchange
682   current density increased from i_o to $3i_o$, b) The CH4 outlet flux at 800 ℃ and 600 ℃ with
683   exchange current density increased from i_o to $3i_o$

684